University of Groningen

Photon dominated regions in NGC 3603 [CI] and mid-J CO line emission

Roellig, M.; Kramer, C.; Rajbahak, C.; Minamidani, T.; Sun, K.; Simon, R.; Ossenkopf, Volker; Cubick, M.; Hitschfeld, M.; Aravena, M.

Link to publication in University of Groningen/UMCG research database

Astronomy & Astrophysics

Photon dominated regions in NGC 3603

[CI] and mid-J CO line emission

M. Röllig[1], C. Kramer[2], C. Rajbahak[1], T. Minamidani[3], K. Sun[1], R. Simon[1], V. Ossenkopf[1,4], M. Cubick[1],
M. Hitschfeld[1], M. Aravena[5], F. Bensch[6], F. Bertoldi[6], L. Bronfman[7], M. Fujishita[8], Y. Fukui[9], U. U. Graf[1],
N. Honingh[1], S. Ito[9], H. Jakob[10], K. Jacobs[1], U. Klein[6], B.-C. Koo[11], J. May[3], M. Miller[1], Y. Miyamoto[9],
N. Mizuno[9,12], T. Onishi[8,9], Y.-S. Park[11], J. Pineda[13], D. Rabanus[14], H. Sasago[9],
R. Schieder[1], J. Stutzki[1], H. Yamamoto[9], and Y. Yonekura[8]

[1] I. Physikalisches Institut, Universität zu Köln, Zülpicher Str. 77, 50937 Köln, Germany
   e-mail: roellig@ph1.uni-koeln.de
[2] Instituto de Radioastronomia Milimetrica (IRAM), Avda. Divina Pastora 7, 18012 Granada, Spain
[3] Department of Physics, Faculty of Science, Hokkaido University, N10W8, Kita-ku, Sapporo 060-0810, Japan
[4] SRON Netherlands Institute for Space Research, PO Box 800, 9700 AV Groningen, The Netherlands
[5] National Radio Astronomy Observatory. 520 Edgemont Road, Charlottesville, VA 22903, USA
[6] Argelander-Institut für Astronomie⋆, Universität Bonn, Auf dem Hügel 71, 53121 Bonn, Germany
[7] Departamento de Astronomía, Universidad de Chile, Casilla 36-D, Santiago, Chile
[8] Department of Physical Science, Osaka Prefecture University, Gakeun 1-1, Sakai, Osaka 599-8531, Japan
[9] Department of Astrophysics, Nagoya University, Furocho, Chikusaku, Nagoya 464-8602, Japan
[10] Deutsches SOFIA Institut, Universität Stuttgart, Pfaffenwaldring 31, 70569 Stuttgart, Germany
[11] Seoul National University, Seoul 151-742, Korea
[12] ALMA-J Project Office, National Astronomical Observatory of Japan, 2-21-1 Osawa, Mitaka, Tokyo 181-8588, Japan
[13] Jet Propulsion Laboratory, M/S 169-507, 4800 Oak Grove Drive, Pasadena, CA 91109, USA
[14] European Southern Observatory, Alonso de Cordova 3107, Vitacura, Casilla 19001, Santiago, Chile

ABSTRACT

Aims. We aim at deriving the excitation conditions of the interstellar gas as well as the local FUV intensities in the molecular cloud surrounding NGC 3603 to get a coherent picture of how the gas is energized by the central stars.

Methods. The NANTEN2-4 m submillimeter antenna is used to map the [CI] 1–0, 2–1 and CO 4–3, 7–6 lines in a $2' \times 2'$ region around the young OB cluster NGC 3603 YC. These data are combined with $C^{18}O$ 2–1 data, HIRES-processed IRAS 60 μm and 100 μm maps of the FIR continuum, and Spitzer/IRAC maps.

Results. The NANTEN2 observations show the presence of two molecular clumps located south-east and south-west of the cluster and confirm the overall structure already found by previous CS and $C^{18}O$ observations. We find a slight position offset of the peak intensity of CO and [CI], and the atomic carbon appears to be further extended compared to the molecular material. We used the HIRES far-infrared dust data to derive a map of the FUV field heating the dust. We constrain the FUV field to values of $\chi = 3-6 \times 10^3$ in units of the Draine field across the clouds. Approximately 0.2 to 0.3% of the total FUV energy is re-emitted in the [CII] 158 μm cooling line observed by ISO. Applying LTE and escape probability calculations, we derive temperatures ($T_{MM1} = 43$ K, $T_{MM2} = 47$ K), column densities ($N_{MM1} = 0.9 \times 10^{22}$ cm^{-2}, $N_{MM2} = 2.5 \times 10^{22}$ cm^{-2}) and densities ($n_{MM1} = 3 \times 10^3$ cm^{-3}, $n_{MM2} = 10^3-10^4$ cm^{-3}) for the two observed molecular clumps MM1 and MM2.

Conclusions. The cluster is strongly interacting with the ambient molecular cloud, governing its structure and physical conditions. A stability analysis shows the existence of gravitationally collapsing gas clumps which should lead to star formation. Embedded IR sources have already been observed in the outskirts of the molecular cloud and seem to support our conclusions.

Key words. ISM: clouds – ISM: structure – ISM: molecules – submillimeter: ISM

1. Introduction

Understanding the feedback between star formation and the interstellar medium (ISM) is important in order to understand the process of star formation (see Zinnecker & Yorke 2007, and references therein). The physical and chemical properties of stars are the heritage of their parental clouds. Stars are born from interstellar gas and release metal-enriched material to the ISM when they die. Radiation from the stars is the prime heating

source for gas and dust in nearby molecular clouds and may trigger velocity and density fluctuations, that stimulate further star formation. To understand the formation of these next generation stars, it is important to understand how the previous generation interacts with its parental clouds (Dale et al. 2005). The energy incident on the clouds in the form of stellar far ultraviolet (FUV: 6 eV$\leq h\nu \leq$ 13.6 eV) radiation is countered by cooling continuum radiation plus emission of atomic fine-structure lines ([CII] 158 μm, [CI] 370 μm, 610 μm, and [OI] 63 μm, 145 μm) and by molecular rotational lines (CO, H_2O, OH, etc.). The cooling emission carries the imprint of the local physical and chemical conditions and can be used to infer

---

⋆ Founded by merging of the Sternwarte, Radiomisches Institut and Institut für Astrophysik und Extraterrestrische Forschung.

the type of environment conducive to maintaining star formation. On their way into a molecular cloud FUV photons are absorbed, and a depth-dependant chemical balance is established. Models of these so-called photon dominated regions (PDRs; see references in Hollenbach & Tielens 1999; Röllig et al. 2007) typically predict a stratification of species like H/H_2, $C^+/C/CO$, and others. This stratification is found to be independent of the shape of the PDR (Gorti & Hollenbach 2002). However, observations often reveal [CI] emission coincident with that of CO (Tatematsu et al. 1999; Ikeda et al. 2002; Mookerjea et al. 2006; Sakai et al. 2006; Kramer et al. 2008; Sun et al. 2008). Plane-parallel models cannot explain this behavior unless full face-on orientation is assumed. Spherical models under isotropic illumination show well-correlated [CI] and CO emission for low density clouds ($n \lesssim 10^4$ cm^{-3}) but predict a limb brightening of the [CI] emission (Röllig et al. 2006). In this work we analyze the distribution of atomic carbon and warm CO in the NGC 3603 star forming region and use LTE approximations and an escape probability model (Stutzki & Winnewisser 1985) to derive the excitation conditions of the gas as well as gas abundances. We refrain from applying more detailed models like the KOSMA-τ PDR model (Störzer et al. 1996; Röllig et al. 2006; Cubick et al. 2008). Recent Herschel/HIFI observations of massive star forming regions provide additional strict constraints on the PDR modeling of these regions, resulting in significantly altered predictions of the local physical and structural conditions (Ossenkopf et al. 2010; Dedes et al. 2010). Hence, we postpone all attempts of PDR modeling in NGC 3603 until the region has been observed with Herschel in the framework of the Herschel Guaranteed Time Key Project *Warm And Dense ISM*.

2. The NGC 3603 star forming region

NGC 3603 is located in the Carina spiral arm ($l \approx 291.6°, b \approx -0.5°$) at a distance of approximately 7–8 kpc (see discussion in Melena et al. 2008). It is one of the most luminous ($L_{bol} > 10^7$ $L_\odot$), optically visible HII regions in the Galaxy, with the massive OB cluster NGC 3603 YC (Young Cluster) as a power source (Goss & Radhakrishnan 1969). The compact core of the cluster was designated HD 97950 due to its star-like appearance. As a comparison, NGC 3603 is 100 times more luminous than the Trapezium cluster in Orion. This young cluster can be considered one of the few Galactic starburst clusters, which are essential for the understanding of extragalactic star bursts. With a dynamic stellar cluster mass of $17\,600 \pm 3800$ $M_\odot$ (Rochau et al. 2010) residing in a cloud of total gas mass of 4×10^5 $M_\odot$ (Grabelsky et al. 1988), it is the most compact Galactic star-forming complex outside the Galactic center region (Stolte et al. 2004). In a number of recent studies, the stellar cluster and the surrounding HII region has been investigated thoroughly (Pandey et al. 2000; Sung & Bessell 2004; Stolte et al. 2006; Lebouteiller et al. 2007, 2008; Harayama et al. 2008; Nürnberger 2008; Crowther et al. 2010). To the south of the cluster we find a giant molecular cloud (see Fig. 1). The intensive radiation and stellar winds from the cluster shape large gaseous pillars at the edge of the cloud (Brandner et al. 2000). CS observations by Nürnberger et al. (2002) show that the molecular gas also extends much further to the north (>10′) and to the south, hosting numerous massive molecular clumps which may be future sites of star formation. A number of prominent IR sources have been found so far (Frogel et al. 1977; Nürnberger 2008; Nürnberger et al. 2010) as well as proplyd like objects (Mücke et al. 2002). Recent AKARI observations of NGC 3603 have been presented by Okada et al. (2010) showing that the [CII] 158 μm emission

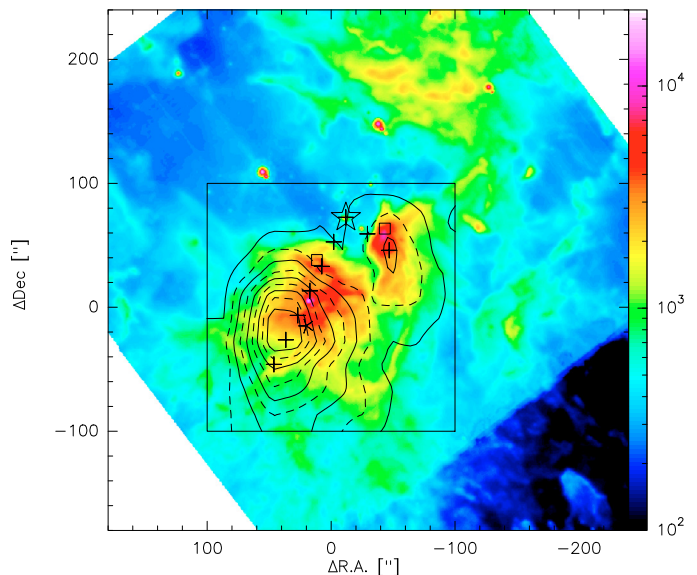**Fig. 1.** 8 μm Spitzer/IRAC band (in MJy/sr) overlayed with CO 4–3 NANTEN2 observations presented in this paper. The position of the cluster is marked by a star. The boxes mark the positions of the pillar heads. The crosses mark the positions along the cuts into MM1 and MM2. IRAC pixel size is 1.2″. The position (0,0) corresponds to RA(J2000.0) = $11^h15^m08.85$, Dec(J2000.0) = $-61°16'50.0$.

is widely distributed and that the [OIII] 88 μm emission follows the MIR, FIR, and radio continuum emission.

3. Observations

We used the NANTEN2-4m antenna at 4865 m altitude in Pampa la Bola in northern Chile to map the central $2' \times 2'$ region of NGC 3603. Our reference position is RA(J2000.0) = $11^h15^m08.85$, Dec(J2000.0) = $-61°16'50.0$, 73″ south-east of the central OB cluster NGC 3603 YC at RA(J2000.0) = $11^h15^m07.26$, Dec(J2000.0) = $-61°15'37.48$. We observed the rotational transitions of ^{12}CO $J = 4-3$ (461.0408 GHz) and $J = 7-6$ (806.6517 GHz) and the two fine-structure transitions of atomic carbon [CI], $^3P_1-^3P_0$ (492.1607 GHz) and $^3P_2-^3P_1$ (809.3446 GHz) (henceforth 1–0 and 2–1), between September and November 2006 with a dual-channel 460/810 GHz receiver. The exact line frequencies were taken from the *Cologne Database for Molecular Spectroscopy* CDMS (Müller et al. 2005, 2001). Double sideband (DSB) receiver temperatures were $\approx$250 K in the lower frequency channel and $\approx$750 K in the upper channel. The intermediate frequencies (IF) are 4 GHz and 1.5 GHz, respectively. The latter IF allows simultaneous observations of the CO 7–6 line in the lower sideband and the [CI] 2–1 line in the upper sideband. These two lines were observed simultaneously with one of the two lower lines in the 460 GHz channel. As backends, we used two acousto optical spectrometers (AOS) with bandwidths of 1 GHz. The channel spacing was 0.37 km s^{-1} at 460 GHz and 0.21 km s^{-1} at 806 GHz. The pointing accuracy was checked regularly on Jupiter, IRC+10216, and IRc2 in OrionA. The applied corrections were always <20″ and usually <10″. To determine the atmospheric transmission, we measured the atmospheric emission at the reference position. Spectra of the two frequency bands were calibrated separately, and side-band imbalances were corrected using the atmospheric model *atm* (Atmospheric Transmission at Microwaves, cf. Pardo et al. 2001). Observations were taken on-the-fly (OTF), scanning in

right ascension at a speed of 2.5″/s and sampling every 10″. The reference position was observed at the beginning of each OTF scanning line.

The half power beam widths (HPBW) deconvolved from the observed full widths at half maximum (*FWHM*) are 38.0″ and 26.5″ in the lower and upper receiver bands, respectively. Beam efficiencies B_{eff} are 50% and 45%, respectively (Simon et al. 2007; Kramer et al. 2008). The median rms across the map is 1.74, 1.53, 0.70, and 1.25 K for CO 4–3, 7–6, [C I] 1–0, and 2–1 respectively. The forward efficiency, F_{eff} = 86% in both bands, was determined from sky-dips. The raw data were calibrated to antenna temperatures T_A^* and scaled to main beam temperatures T_{mb} with the factor F_{eff}/B_{eff}. We present all data in units of T_{mb}. Fifth order polynomial baselines were subtracted from all spectra. Observations of the atomic carbon lines are very challenging and require many OTF coverages to achieve a signal to noise (S/N) ratio above 3σ.

4. Data

4.1. Dust and PAHs

In Fig. 1, we show a map of integrated CO 4–3 intensities from NANTEN2 overlaid to an 8 μm image taken with the Infrared Array Camera (IRAC) on board the Spitzer space telescope[1]. The position of the OB cluster is marked by a star. The image shows prominent molecular clumps southwest and southeast of the cluster position. Following Nürnberger et al. (2002), we refer to them as MM1 and MM2, respectively. The IRAC image shows the sharp PDR interfaces between the HII region and the molecular cloud. The positions of these interfaces match the pillar-like structures visible in HST and VLT images (Brandner et al. 2000). Note that these pillars are much smaller than the molecular clouds from which they protrude. We also note a dusty filament, which connects MM1 and MM2 in a large arc 1.5′ to 2′ south of the western pillar head. This filament is not visible in CO or [CI] emission. The strong 8 μm emission ($>10^4$ MJy/sr) includes strong PAH emission (7.6, 7.8, and 8.6 μm). The 8 μm band is an excellent tracer of the PDR interface. For a detailed analysis of the emission by PAH's and very small grains see Lebouteiller et al. (2007).

4.2. NANTEN2 observations

4.2.1. Maps of integrated intensity

Figure 2 shows maps of integrated CO 4–3, 7–6, [C I] 1–0, and 2–1 emission integrated over a velocity range from 4 to 26 km s^{-1}. The two molecular clumps MM1 and MM2 are visible: MM1 to the southwest of the OB cluster and MM2 to the southeast. The peak intensities are 267 K km s^{-1} for CO 4–3, 121 K km s^{-1} for CO 7–6, 28 K km s^{-1} for [C I] 1–0, and 30 K km s^{-1} for [C I] 2–1.

MM2 is very prominent in all 4 observed transitions while MM1 is weaker in the fine structure transitions.

Both CO maps mark the transition from the HII region to the molecular cloud. MM1 is presumably smaller than our beam size (Nürnberger et al. 2002), hence it is not possible to infer detailed structure information from the maps.

The observed intensity distributions of the [C I] fine structure transitions are more extended with a lower contrast in
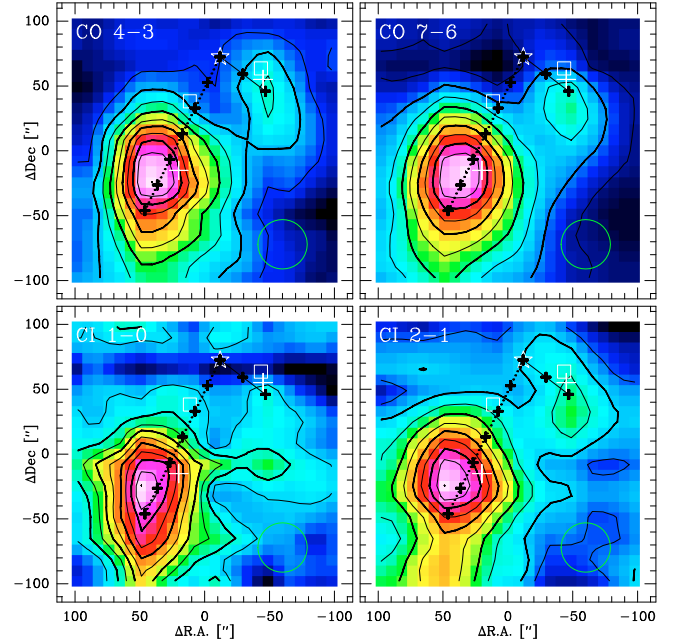
Fig. 2. Velocity integrated maps (200″ × 200″) of CO 4–3, 7–6, [C I] 1–0, and 2–1 smoothed to a common angular resolution of 38″ (1.3–1.5 pc at 7–8 kpc), and integrated over a velocity range from 4 to 26 km s^{-1}. Color scale and contours show the same data. Contours range between 10 and 90% of the peak intensities which are 267 K km s^{-1} for CO 4–3, 121 K km s^{-1} for CO 7–6, 28 K km s^{-1} for [C I] 1–0, and 30 K km s^{-1} for [C I] 2–1. The position of the compact OB cluster is marked by a white star. The position of the the pillars, as seen in the HST images, are marked by white squares. Dashed lines and small crosses spaced by 22″ mark two cut from the OB cluster to the peak positions of the two clumps MM1 (short cut) and MM2 (long cut). The circle marks the resolution and the two white crosses mark the position of the CS(2–1) peaks (Nürnberger et al. 2002) in MM1 and MM2. The position (0, 0) corresponds to RA(J2000.0) = 11^{h}15^{m}08^s.85, Dec(J2000.0) = −61°16′50″.0.

comparison to the intensity distributions of the CO rotational line transitions. The peak positions of [CI] are slightly shifted away from the cluster compared to CO. However, the S/N of both [C I] transitions is too low to allow further conclusions. MM1 can be identified in both CO maps. In [C I] a diffuse emission is visible without a clear distinction between clump center and its more diffuse environment. The MM2 peak positions of both CO maps match within the pointing accuracy. The same is true for both [C I] maps. Both [C I] peaks are shifted away from the OB cluster with respect to CO. However, we note a good spatial correlation between the CO and [C I] emission as all peaks coincide within a beam radius. We do not see any C-CO layering as expected from simple edge-on, plane-parallel PDR scenarios. It is possible to explain coincident [C I] and CO emission with a face-on configuration, but the visible pillar structures in the HST observations and the very sharp interface visible in the IRAC image in Fig. 1 clearly show a prominent, edge-on PDR interface.

The velocity structure of the observed field is shown in the CO 4–3 velocity channel maps (Fig. 3). From the channel maps, it is evident that the emission towards MM1 shows a smaller kinematic range than in MM2. MM1 is not observable at velocities higher than 16 km s^{-1}, while the emission in MM2 extends up to 21 km s^{-1}. At larger velocities, the emission gradually shifts to the southwest. A similar kinematic behavior is also visible from CS (3–2) observations by Nürnberger et al. (2002). Their results also show a velocity drift for MM1 with distance

Table 1. Observed integrated intensities $I = \int T_{mb}\, dv$ in units of K km s^{-1}, v_{LSR} in units of km s^{-1}, and the line widths *FWHM* in units of km s^{-1} computed as 0th, 1st, and 2nd moment of the spectra between $v = 8...22$ km s^{-1}.

$\Delta\alpha/\Delta\delta$ ['' /'']	I_{43} [K km s^{-1}]	Δv_{43} [km s^{-1}]	v_{LSR} [km s^{-1}]	I_{76} [K km s^{-1}]	Δv_{76} [km s^{-1}]	v_{LSR} [km s^{-1}]	I_{10} [K km s^{-1}]	Δv_{10} [km s^{-1}]	v_{LSR} [km s^{-1}]	I_{21} [K km s^{-1}]	Δv_{21} [km s^{-1}]	v_{LSR} [km s^{-1}]
10/30	48	3.5	13.2	29	8.2	13.9	6	7.4	14.5	7	10.0	15.7
20/10	153	6.7	14.2	71	7.4	13.5	12	8.2	13.6	14	7.8	15.0
30/–10	252	7.8	14.9	119	7.5	13.6	27	7.1	14.6	24	6.1	14.6
40/–30	267	8.4	15.2	121	7.8	13.7	27	5.2	14.2	30	7.1	14.1
50/–50	175	7.1	14.8	84	7.7	13.8	26	7.2	14.3	20	6.4	14.3
–30/60	57	4.9	15.0	24	7.5	13.0	0	0.0	50.1	6	3.7	16.3
–50/50	90	6.0	13.8	40	7.7	13.3	11	8.4	13.5	9	6.9	14.7

Notes. The positions lie along a line starting from the OB cluster. The cluster position has been omitted. Rotational transitions of CO are denoted 43 (^{12}CO 4–3) and 76 (^{12}CO 7–6). The atomic carbon fine-structure transitions are denoted 10 ($^3P_1 - {}^3P_0$) and 21 ($^3P_2 - {}^3P_1$).
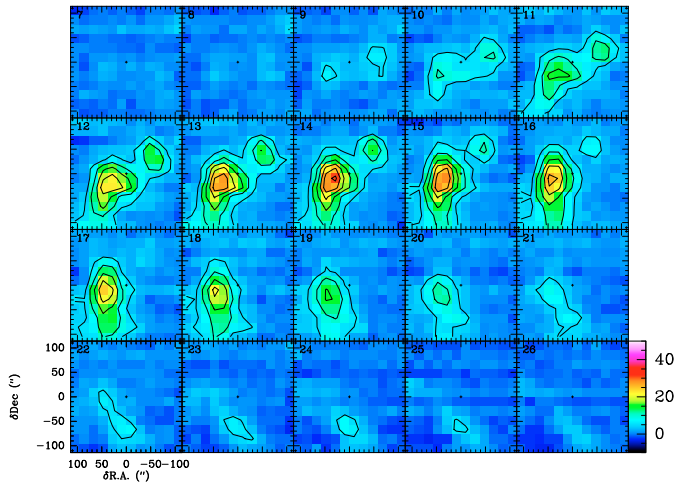

Fig. 3. Velocity structure of the observed field: CO 4–3 intensity in velocity channels of 1 km s^{-1} width. Contours range between 5 and 45 K in steps of 5 K. The position $(0, 0)$ corresponds to RA(J2000.0) = 11^{h}15^{m}08^{s}85, Dec(J2000.0) = $-61°16'50''0$.

Fig. 4. Spectra along two cuts connecting the OB cluster and the centre of MM1 (*bottom*) and MM2 (*top*). The CI spectra appear to show sinusoidal standing waves, however a detailed analysis shows no consistent standing wave pattern. These baseline variations are thus attributed to instabilities of the system and/or the atmosphere during the measurements. All data are at a common resolution of 38'' and on the main beam temperature scale.

4.3. Analysis

4.3.1. LTE – Column densities and temperatures

In Table 2 we give the velocity integrated line ratios R_{74} (I_{76}/I_{43}), R_{21} (I_{21}/I_{10}) and R_{14} (I_{10}/I_{43}) for all positions along the two cuts. We compute the LTE temperatures using the optically thick CO 4–3 emission assuming a beam filling of 1 and obtain temperatures of 42 K for the peak position in MM2 and 24 K for MM1. This is roughly consistent with estimates from the [C I] line ratio. R_{21} is a sensitive function of the [C I] excitation temperature. In the optically thin limit and assuming LTE, $T_{ex} = 38.3$ K/ln[2.11/R_{21}]. In MM2 we find ratios between 0.8 and 1.1 which correspond to temperatures between 40 and 60 K. For MM1 the [C I] line ratio gives a temperature estimate of 42 K, higher than the estimate derived from the CO 4–3 emission. The difference can be explained by beam dilution effects since MM1 is not resolved within the NANTEN2 beam. However, the atomic carbon emission is heavily affected by noise. Another possibility is to use the LTE ratio of the two optically thick lines R_{74} to derive an excitation temperature: $T_{ex} = 99$ K/ln[3.06/R_{74}]. R_{74} is remarkably constant across both clouds. We find an excitation temperature slightly above 50 K for both clouds. First, this confirms that both clouds have comparable excitation conditions despite their different appearance. Second, they seem not to be composed of hot, unresolved clumps which would result in

from the OB cluster, possibly indicating a placement of MM1 in front of the cluster. In the appendix we show the velocity channel maps of the remaining 3 transitions.

4.2.2. Spectra along a cut through the region

To study the transition from the ionized to the molecular gas, we selected two cuts from the OB cluster to the peak positions of MM1 and MM2. The positions along the cut are 22'' apart and marked in Fig. 2. The spectra along the two cuts, shown in Fig.4, trace the kinematic structure of the interface regions and the molecular clumps. The spectra at the positions 30''/–10'', 40''/–30'', and 50''/–50'' do not show simple Gaussian line profiles. Nürnberger et al. (2002) observed similar line profiles in their CS 3–2 and 2–1 observations of MM2. They used two Gaussian components separated by 3 km s^{-1} to fit the emission profiles. Our analysis showed that it is not possible to use a similar two component Gaussian fit to reproduce our observations at all positions. We derived the first three moments of the spectral line, i.e., integrated intensity, mean velocity, and *FWHM*, over the channels in the range $v = 6$–22 km s^{-1}. The derived moments are given in Table 1. At the offsets –10''/70'' and 0''/50'' we don't find sufficient emission to derive significant values.
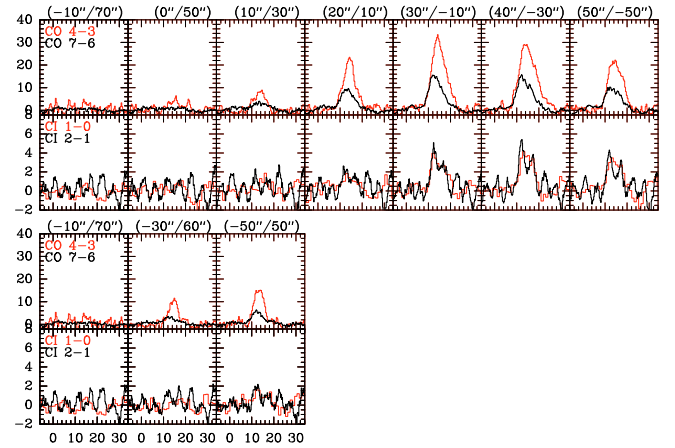
Table 2. Line ratios R_{74} (I_{76}/I_{43}), R_{21} (I_{21}/I_{10}) and R_{14} (I_{10}/I_{43}) for all positions along the two cuts.

$\Delta\alpha/\Delta\delta$	R_{74}	R_{21}	R_{14}	$T_{ex,43}$	$T_{ex,74}$	N_C	$\int T_{mb}(C^{18}O)dv$	$N_{C^{18}O}$	N_{tot}	$N(C)/N_{tot}$	M_{LTE}	M_{vir}
['' /'']				[K]	[K]	cm^{-2}	[K km s^{-1}]	[10^{15} cm^{-2}]	[10^{21} cm^{-2}]		[$M_\odot$]	[$M_\odot$]
10/30	0.62	1.15	0.14	23	62	9.5×10^{16}	1.6	2.27	11.35	8.4×10^{-6}	236	208
20/10	0.47	1.09	0.08	33	53	1.7×10^{17}	1.9	3.57	17.83	9.7×10^{-6}	371	751
30/–10	0.47	0.91	0.11	43	53	3.9×10^{17}	4.2	9.84	49.19	7.9×10^{-6}	1024	1006
40/–30	0.45	1.09	0.10	42	52	4.1×10^{17}	4.3	9.87	49.36	8.2×10^{-6}	1028	1175
50/–50	0.48	0.79	0.15	34	54	3.7×10^{17}	2.1	4.04	20.20	1.9×10^{-5}	421	845
–30/60	0.43	8.89	0.01	21	51	$1. \times 10^{17}$	1.3	1.73	8.64	1.2×10^{-5}	180	399
–50/50	0.44	0.84	0.12	24	51	1.5×10^{17}	2.1	3.07	15.37	$1. \times 10^{-5}$	320	599

Notes. The LTE excitation temperature $T_{ex,43}$ is derived from the optically thick I_{43} emission, $T_{ex,74}$ is derived from R_{74} The C column densities are derived assuming LTE and optically thin [C I] emission. Values of the integrated intensities of $C^{18}O$ 2–1 are given as presented in Nürnberger et al. (2002) along the two cuts, the LTE excitation temperature is derived from I_{43}. The LTE column densities of $C^{18}O$, and the total gas column density assume an isotope ratio of 500 and CO:H_2 = 8×10^{-5} (Frerking et al. 1982), i.e. a ratio of C18O/H_2 = 2×10^{-7}.

a much higher excitation temperature derived from R_{74}. Instead the gas appears to be more smoothly distributed and excited.

The atomic carbon column density was derived under the assumption of LTE and optically thin [C I] emission. To derive the total H_2 column densities we use the integrated intensity of $C^{18}O$ 2–1 as presented in Nürnberger et al. (2002). Assuming optically thin emission, an isotope ratio of 500 and CO:H_2 = 8×10^{-5} (Frerking et al. 1982), i.e., an assumed ratio of $C^{18}O/H_2$ = 2×10^{-7}, we compute the column densities along the two cuts. The results are summarized in Table 2. For MM1, we find a total column density of 1.5×10^{22} cm^{-2}; for MM2, N = $2...5 \times 10^{22}$ cm^{-2}. We find that the relative abundance of atomic carbon N_C/N_{tot} drops towards the peak positions with values of 10^{-5} (MM1) and $8-19 \times 10^{-6}$ (MM2), and increases at positions towards as well as away from the OB cluster. Even though the spatial resolution of our maps is rather coarse, this could be an indication for a C/CO stratification, because in this case we would expect limb brightened [CI] emission. The gas pressure within MM1 and MM2 (assuming a density of 10^4 cm^{-3}) is about 10–30% of the pressure in the HII region (Shaver & Goss 1970). Hence, the interface region is compressed and driven against the molecular cloud, visible, e.g., in the pillars protruding from MM1 and MM2. From the total column density we can estimate the total mass per beam. The results are given in Table 2. We also derived virial mass estimates across the cuts assuming a density of 10^4 cm^{-3} and kinetic temperatures of 50 K (the densities are in agreement with the calculations from Sect. 4.3.3). The virial masses agree very well with the LTE masses and are much larger than the Jeans mass of the material of 87 $M_\odot$. This means, the gas is gravitationally bound and not transient. We expect that the strong HII pressure and the gravitational instability causes strong fragmentation and cloud collapse. Nürnberger et al. (2002) derived a star formation efficiency of $\geq$30% and a mean star formation rate of 1.3×10^{-3} $M_\odot$ yr^{-1}. Embedded IR sources have already been identified (Frogel et al. 1977) along the outskirts of the molecular clouds and particularly at the base of the pillar like structures at the edge of MM2 (Nürnberger 2008; Nürnberger et al. 2010).

4.3.2. Dust temperatures and FUV intensities

To estimate the total FUV flux, we consider the total luminosities of the most massive O stars in the central OB cluster. Recently, Melena et al. (2008) published an updated census of the massive star content of NGC 3603. The most massive members of the OB cluster are 3 WNL stars, 14 O3(and 3.5) stars (III+V) and at least 20 late O-type stars. They produce the FUV flux that

dominates the heating of the PDRs and the molecular clouds. At an effective temperature of 24 000 K, the ratio of the FUV energy density to the total energy density emitted by the star $\Phi_{FUV}/\Phi_{tot} \approx 0.7$ is maximal if we assume pure black body emission. At higher temperature, relatively more energy is emitted in the EUV range (13.6 eV < $h\nu$ < 130 eV)[2].

Applying effective temperatures and luminosities as given by Martins et al. (2005) for the O stars, Panagia (1973) for the B stars and Crowther (2007) for the WR stars, we calculated a total FUV luminosity of 1.1×10^{43} erg s^{-1} from the contribution of each cluster member. This is a lower limit since the spectral classes for more than 10 cluster members remains unknown. Depending on the distance from the cluster center d, in units of pc, the FUV flux is $\chi = 9.4 \times 10^4 d^{-2}$ in units of the Draine field. At a distance of 7–8 kpc, one parsec corresponds to angular distances of 26–29'', i.e., somewhat smaller than the projected distance between the cluster center and the edge of MM2 as seen for example in Fig. 1 ($\approx$46''). If we assume that the cluster and the molecular cloud are situated in the same plane, the FUV field at the peak position in MM2 drops to $\chi \approx$ 5000–6600. This is of the same order as the flux at the MM2-peak derived from the IRAS data. If the clumps are displaced from the plane of the OB cluster, or if the distance to the complex is different, the derived χ changes. Uncertainties in the in-plane displacement of $\pm$4 pc and in the distance (7–8 kpc) lead to χ = 2400–6600.

We use IRAS data to derive dust temperatures and the FUV continuum in the observed region. Enhanced resolution images of $\sim$1' resolution were created using the maximum correlation method (Aumann et al. 1990). We estimate dust temperatures from the ratio of HIRES 60 μm and 100 μm data, assuming a dust spectral index of emissivity of 1.5. We obtained high resolution (HIRES) 60 and 100 μm images (2°×2°) from the IPAC data center[3]. Along the two cuts, we find almost constant dust temperatures of 35 K. This value is very close to the dust temperature of 37 K derived from MSX data by Wang & Chen (2010). Again, comparison with the higher resolution Spitzer maps shows that the warm dust is not distributed homogeneously. We conclude that the HIRES data are, therefore, affected by beam filling.

Following Nakagawa et al. (1998), we combined 60 and 100 μm data to create a map of far-infrared intensities between 42.5 μm and 122.5 μm (Helou et al. 1988). Under the assumption

---

[2] Pauldrach et al. (1998) showed in model calculations that for effective temperatures below 45 000 K, the ratio of FUV to EUV photon rates is considerably higher than the ratio derived for pure blackbody spectra (see also Brandner et al. 2000). This is because EUV photons are absorbed in the ionization front. We neglect this effect.
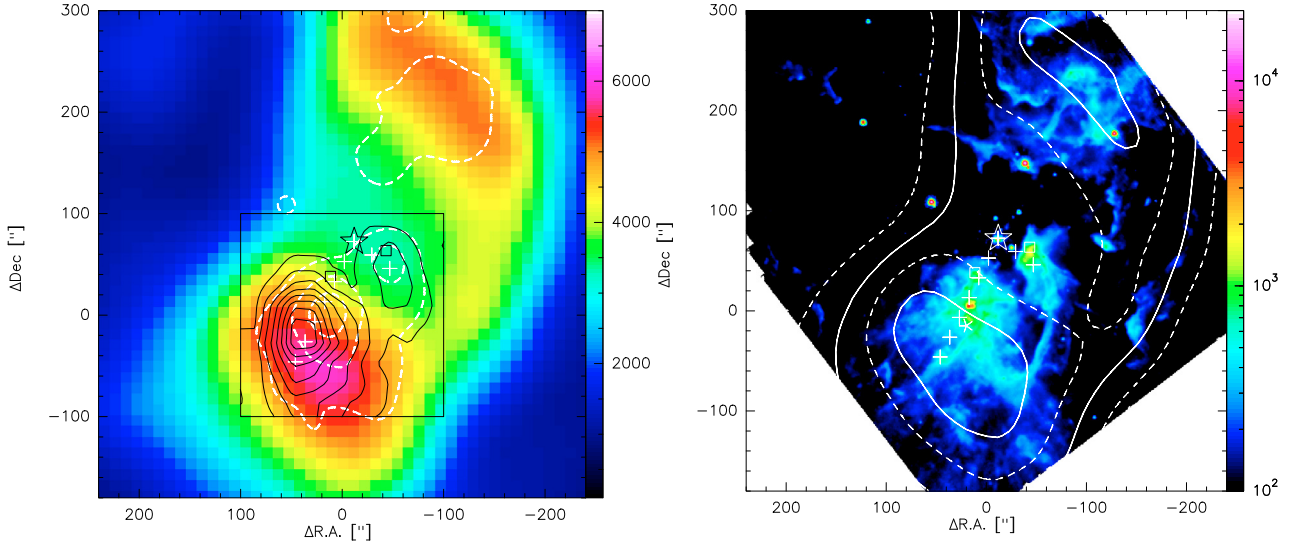
[3] http://www.ipac.caltech.edu/

Fig. 5. *Left*: values of the FUV field in units of the Draine field derived from the HIRES 60, and 100 μm fluxes as color map. White, dashed contours mark the Spitzer/IRAC 5.8 μm flux smoothed to a resolution of 35″. The contour values are 25, 50, and 75% of the peak value. Overlayed in thin contours is the NANTEN2 CO 4–3 map. The central OB cluster is marked by a star. The two pillar heads are denoted by the squares, White crosses mark the positions along the cuts into MM1 and MM2. *Right*: spitzer/IRAC 5.8 μm observation (in MJy/sr) overlayed with FUV fluxes as derived from IRAS/HIRES flux ratios. The contours correspond to values of $\chi = 2000, 3000, 4000,$ and 5000. IRAC pixel size is 1.2″. The position (0,0) in both panels corresponds to RA(J2000.0) = $11^{h}15^{m}08.85$, Dec(J2000.0) = $-61°16'50.''0$.

that all FUV energy absorbed by the grains is re-radiated in the far-infrared (FIR), we compute the FUV fluxes (χ) from the emergent FIR intensities (cf. Kramer et al. 2005) I_{FIR}, using $\chi/\chi_0 = 4\pi\, I_{FIR}$, with $\chi_0 = 2.7 \times 10^{-3}$ erg s^{-1} cm^{-2} (Draine 1978). The resulting map of the FUV continuum is shown in the left panel of Fig. 5. Overlayed as thin contours is the NANTEN2 CO 4–3 map. At the peak position of MM1, we find FUV fields of $\chi = 3460$. Along the cut in MM2, we find that χ gradually increases from 3350 at the position of the OB cluster to 5230 at the peak position. Due to the low spatial resolution of the HIRES data, these values are lower limits since beam dilution effects are not negligible.

One would expect a decrease of FUV with growing distance from the cluster. However, such a decrease is not seen, Fig. 5 shows the opposite. This is because the method of deriving FUV intensities from IRAS data is not working for too small dust column densities because then UV radiation can not be effectively transformed to IR. Consequently, it would be best to exclude these parts from the further analysis. In our case, this is impossible due to the large beam. HIRES beam sizes vary from $\sim$35″ to over 120″ across the maps, hence the FUV values in Fig. 5 are considerably beam diluted. In the right panel of Fig. 5, we overlayed the FUV fields derived from the HIRES data on 5.8 μm Spitzer/IRAC observations of NGC 3603 to illustrate the beam filling effect: 60 and 100 μm emission can only be measured if dust is present at all. The Spitzer map shows no dust emission between the interface and the cluster. The HIRES beam size at the cluster position is almost circular with a *FWHM* of $\sim$35″. Hence, a contribution to the IRAS/HIRES fluxes at the cluster position can only come from the interface regions of MM1 and MM2. If 60/100 μm emission could be measured at 1–2″ resolution, one could not determine the FUV field towards the cluster and would observe a sharp interface between the H II region and the clumps. Instead we see no zero FUV intensity at the cluster and a gradual increase up to the peak 80″ behind the interface. This is further illustrated in the left panel in Fig. 5 where we additionally overlayed Spitzer/IRAC 5.8 μm emission smoothed to the best HIRES resolution of 35″. At this

resolution, up to 50% of the total flux is smeared across the H II region.

At the MM2-peak, the HIRES beam is almost fully filled and the FUV fluxes are consistent with the assumption that the molecular cloud and the cluster lies in almost the same plane of the sky. This also supports the assumption that the FUV irradiation of the OB cluster created the pillars seen in the HST/VLT images.

The derived FUV fluxes can be used to estimate the ratio I_{CII}/I_{FUV}, i.e. the fraction of FUV energy that is re-emitted in the the [CII] 158 μm cooling line. We retrieved the [CII] spectrum[4] from the ISO data archive[5] and compute an integrated intensity of 2×10^{-3} erg s^{-1} cm^{-2} sr^{-1}. Most of the FUV energy that irradiates the cloud is re-radiated in the continuum, but a small fraction is re-emitted in cooling lines, such as the [CII] 158 μm line. Applying the FUV flux derived from the HIRES data, we estimate $I_{CII}/I_{FUV} \approx 0.2...0.3\%$. This is consistent with similar results from regions of active star formation, e.g., nuclear regions of galaxies, where approximately 0.1 to 1% of the total FUV input is re-radiated in the [CII] line (Stacey et al. 1991). However, this remains a rough estimate because of the large beam sizes involved.

Considering the similar FUV estimates from stellar luminosities and from the FIR data, we conclude that the FUV flux illuminating the molecular clumps MM1 and MM2 is 3000–6000 in units of the Draine field. Approximately 0.2 to 0.3% of the total FUV energy is re-emitted in the [CII] 158 μm cooling line.

4.3.3. Escape probability – density and temperatures

We performed escape probability (EP) calculations (Stutzki & Winnewisser 1985) to derive local gas densities, column densities, and gas temperatures from the observed line ratios (R_{74}, R_{21}, R_{14}, and $I_{C^{18}O2-1}/I_{43}$). The model assumes a finite, spherical cloud geometry. We fitted the column densities of ^{12}CO

---

[4] Taken at RA(J2000.0) = $11^{h}15^{m}10.2$, Dec(J2000.0) = $-61°16'45.''52$, FITS file name: lsan20100302.fits

[5] http://isowww.estec.esa.nl/ida/

Table 3. Results from the escape probability calculations.

$\Delta\alpha/\Delta\delta$ ['']/['']	T [K]	n [cm^{-3}]	f	N_{CO} [10^{17} cm^{-2}]	N_C [10^{17} cm^{-2}]	N_{tot} [10^{21} cm^{-2}]	$N_{tot} \times f$ [10^{21} cm^{-2}]	M_{EP} [$M_\odot$]	$\langle n \rangle$ [cm^{-3}/beam]
10./30.	53	$3. \times 10^3$	0.112	28.3	4.6	33.3	3.7	693	9775
20./10.	48	5.2×10^3	0.277	23.7	5.8	27.9	7.7	581	8197
30./−10.	49	4.5×10^3	0.429	43.3	12.3	51.0	21.8	1061	14969
40./−30.	47	1.6×10^4	0.665	32.3	12.4	38.0	25.3	791	11154
50./−50.	42	9.2×10^3	0.383	19.5	12.3	22.9	8.8	477	6734
−30./60.	65	$3. \times 10^3$	0.125	26.8	9.0	31.5	4.0	657	9262
−50./50.	43	$3. \times 10^3$	0.187	38.5	6.1	45.2	8.5	942	13288

Notes. The filling factor $f = I_{obs}/I_{mod}$ is derived from the CO 4–3 intensities. The CO and C column densities are results from the escape probability fit.

and C independently. From the absolute CO 4–3 intensities we derived a filling factor I_{obs}/I_{mod}. The total H$_2$ column densities and masses have been calculated using CO:H$_2 = 8 \times 10^{-5}$. The results are shown in Table 3.

For MM2, the temperatures from the EP calculations agree within 25% with the LTE temperatures for the positions 30''/−10'', 40''/−30'', and 50''/−50''. Masses and column densities are comparable with results from the LTE calculations. The filling factor is roughly 0.3–0.6 across MM2. MM1 shows significantly smaller values of 0.1−0.2. This is consistent with the morphology namely that the clouds are clumpy and MM1 is not resolved by the NANTEN2 beam. The derived temperatures for MM1 are about a factor 2 larger compared to the temperatures derived from CO 4–3 and are compatible with the temperatures derived from the observed ratio R_{74} (consistent with $f < 1$). The gas densities found for MM1 and MM2 are about 10^4 cm^{-3}. In contrast to the LTE results, we find a monotonously growing N_C/N_{H_2} along the cut in MM2 with values of $1-5 \times 10^{-5}$. The column densities, given in Table 3, result in C/CO abundance ratios between 0.16–0.6 Similar abundance ratios have been observed in other Galactic star forming regions like CepheusB, Orion or NGC 7023 (see references in Mookerjea et al. 2006). The C/CO ratio is supposed to depend on the local FUV intensity due to dependency of the CO formation and destruction balance on the FUV illumination. Sun et al. (2008) found significantly lower C/CO ratios in IC 348 where the FUV field varies between 1 and 100 Draine units. On the other hand, Kramer et al. (2008) found C/CO ratios comparable to our results in the Carina region, where the FUV field is also comparable to NGC 3603. We also find a monotonously growing C/CO abundance ratio along the cut in MM2. A similar trend has been found by Mookerjea et al. (2006), namely that the C/CO ratio is higher further away from the sources of FUV radiation.

5. Summary and conclusions

We used the NANTEN2-4m telescope to map the emission of atomic carbon and CO in the vicinity of the central OB cluster in the Galactic star forming region NGC 3603. These data are the first observations of CO 4–3, CO 7–6, [CI] 1–0, and [CI] 2–1 in NGC 3603. We present fully sampled 200'' × 200'' maps integrated over the full velocity range as well as velocity channel maps. The observed field includes the central OB cluster, as well as the two adjacent molecular clumps MM1 and MM2, hosting two pillars observed by the HST and similar in appearance to the famous pillar structures in the M16 nebula. We selected two cuts from the OB cluster position to the peak emission in MM1 and MM2 for detailed analysis. The spectra along the two cuts show a rich kinematic structure, especially towards MM2. The observed maps show a strong correlation between

the spatial distribution of C and CO. This implies either a face-on configuration of the clouds, i.e., both clouds being not in the same plane as the OB cluster and thus being illuminated face-on, or a more complex configuration, for instance a composition of many small clumps. The overall good C-CO correlation may indicate an unresolved, clumpy structure, but the increase of N_C towards a cloud edge could hint towards relatively well shielded inner parts.

Using escape probability model calculations we derived temperatures, densities, and column densities for both clouds from the observed line ratios. The temperatures are 43 K and 47 K for the peak positions of MM1 and MM2, respectively. We find gas densities of $n = 10^3 - 10^4$ cm^{-3} in MM1 and MM2. From the best fit CO column densities we derive total H$_2$ column densities (filling corrected) of 0.9×10^{22} cm^{-2} and 2.5×10^{22} cm^{-2} for MM1 and MM2 and a ratio of N_C/N_{H_2} of $1-5 \times 10^{-5}$.

The cluster is strongly interacting with the ambient molecular cloud and governing its structure and physical conditions. The stability analysis shows the existence of gravitationally bound gas which should lead to star formation. Embedded IR sources have already been observed in the outskirts of the molecular cloud and support our conclusions.

We used HIRES/IRAS far-infrared data to narrow down the value of the FUV field at the positions of the two molecular clouds. Consistent with estimates from spectral type approximations and with [CII] observations by ISO we find $\chi \approx 3-6 \times 10^3$ in units of the Draine field.

However, many issues remain unresolved. For example, the analysis results are not conclusive regarding the clumpiness of the gas. NGC 3603 will be observed within the Herschel Guaranteed Time Key project *Warm and Dense ISM – WADI*. These data will allow us to perform a much more detailed study of the local gas conditions. Cooling lines like [O I] and [C II] as well as high-*J* CO lines can be used to study the clumpiness and the energy balance of the gas.

Appendix A: Velocity channel maps

Here we present the velocity channel maps of all observed transitions. Each map is shown at its original spatial resolution, i.e. 38'' for CO 4–3 and CI 1–0 as well as 26.5'' for CO 7–6 and CI 2–1.
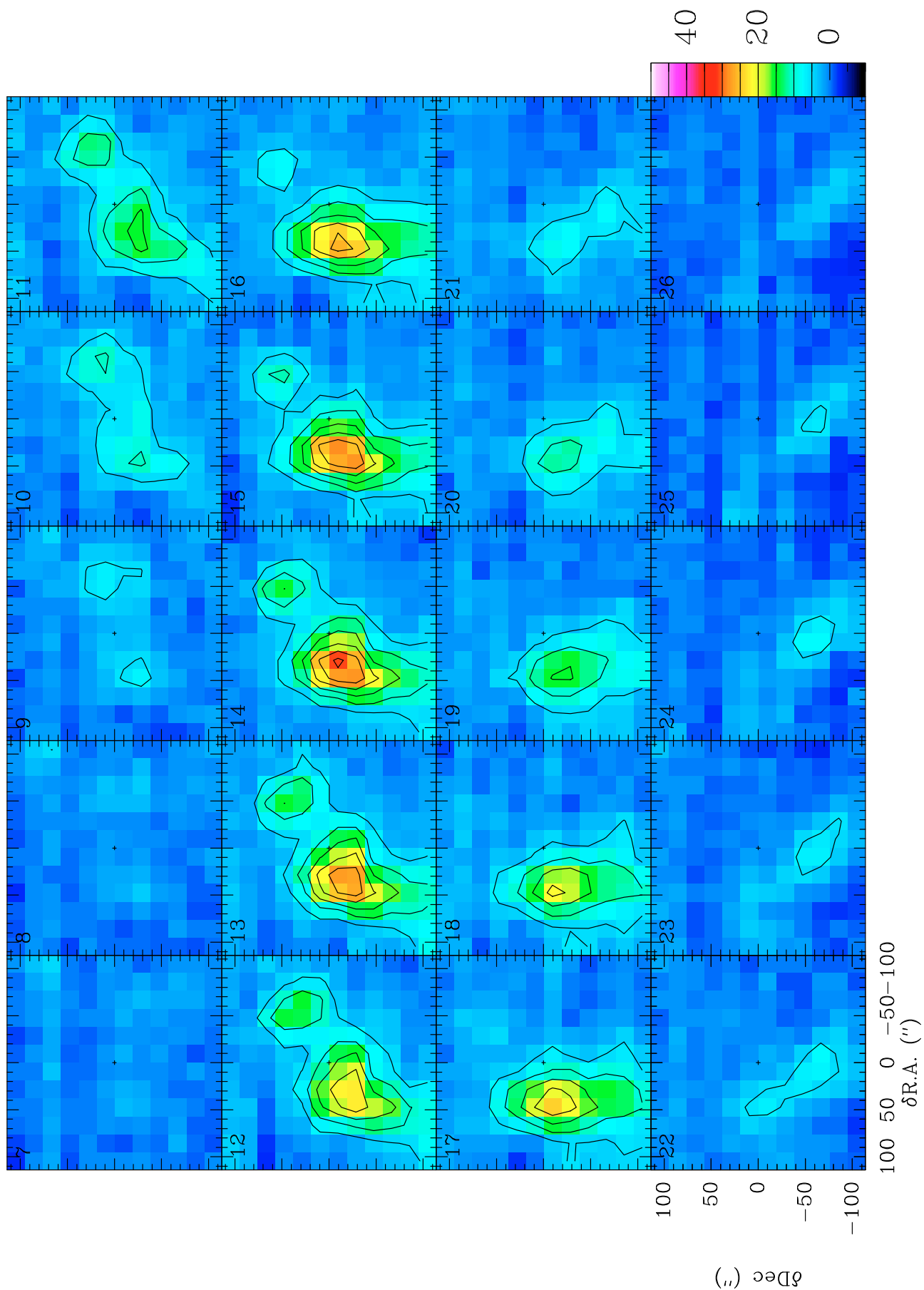
Fig. A.1. Velocity structure of the observed field: CO 4–3 intensity in velocity channels of 1 km s^{-1} width. Contours range between 5 and 45 K in steps of 5 K. The position $(0, 0)$ corresponds to RA(J2000.0) = 11^{h}15^{m}08^s.85, Dec(J2000.0) = −61°16′50″.0.
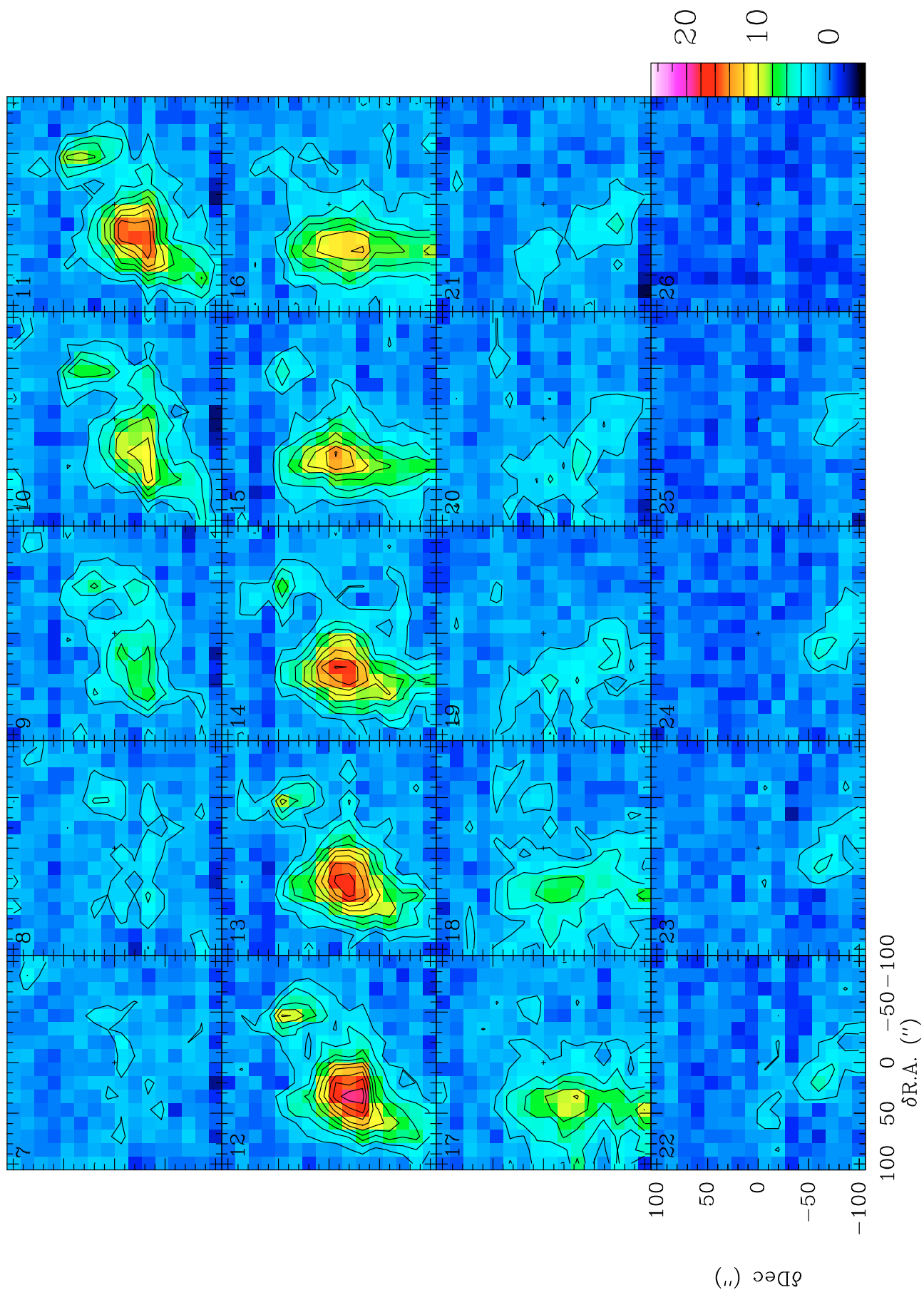
Fig. A.2. Velocity structure of the observed field: CO 7–6 intensity in velocity channels of 1 km s^{-1} width. Contours range between 2 and 20 K in steps of 2 K. The position $(0, 0)$ corresponds to RA(J2000.0) = 11^{h}15^{m}08^s.85, Dec(J2000.0) = $-61°16'50''.0$.
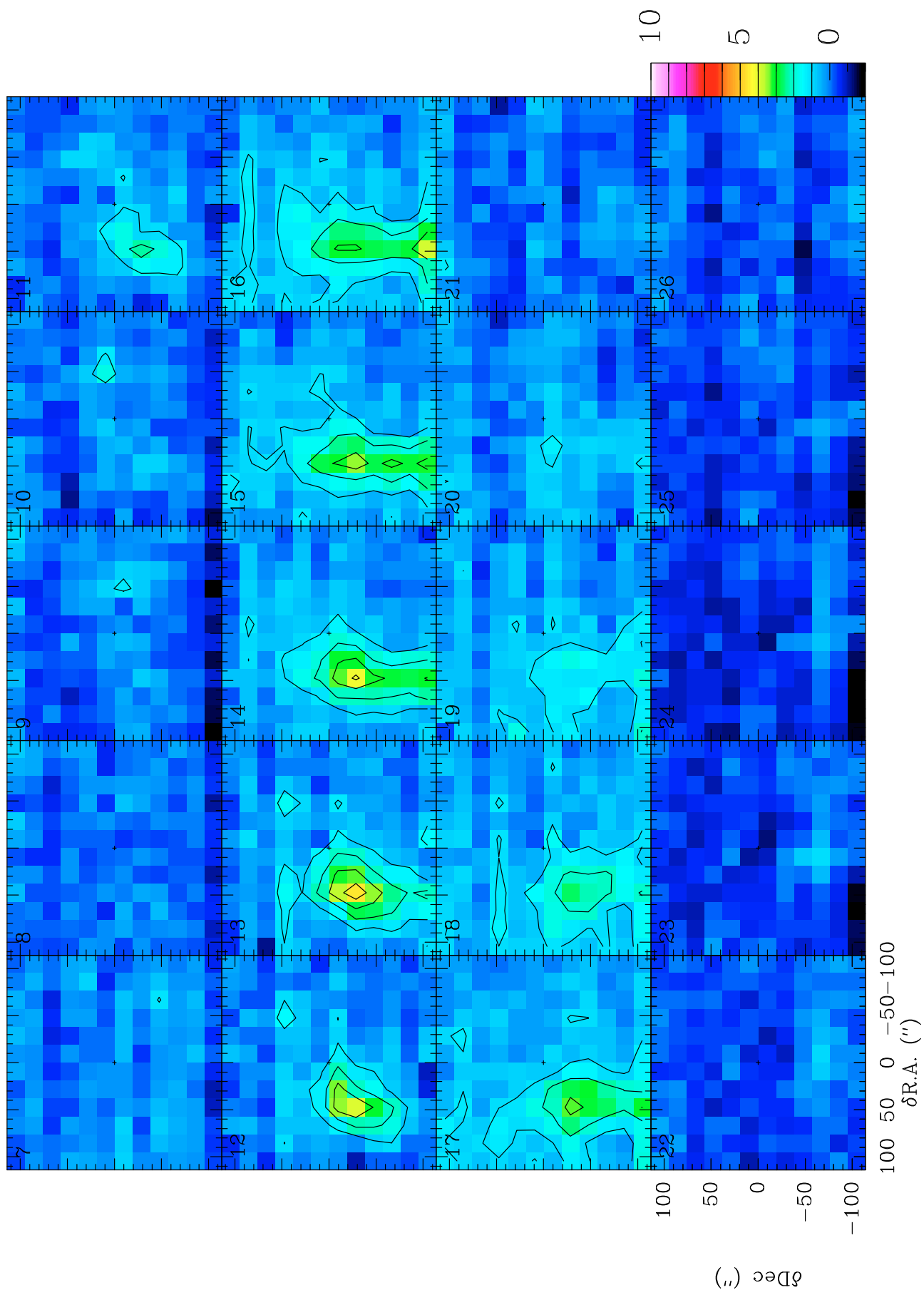
Fig. A.3. Velocity structure of the observed field: [CI] 1–0 intensity in velocity channels of 1 km s^{-1} width. Contours range between 1 and 10 K in steps of 1 K. The position $(0, 0)$ corresponds to RA(J2000.0) = $11^h15^m08^s.85$, Dec(J2000.0) = $-61°16'50''.0$.
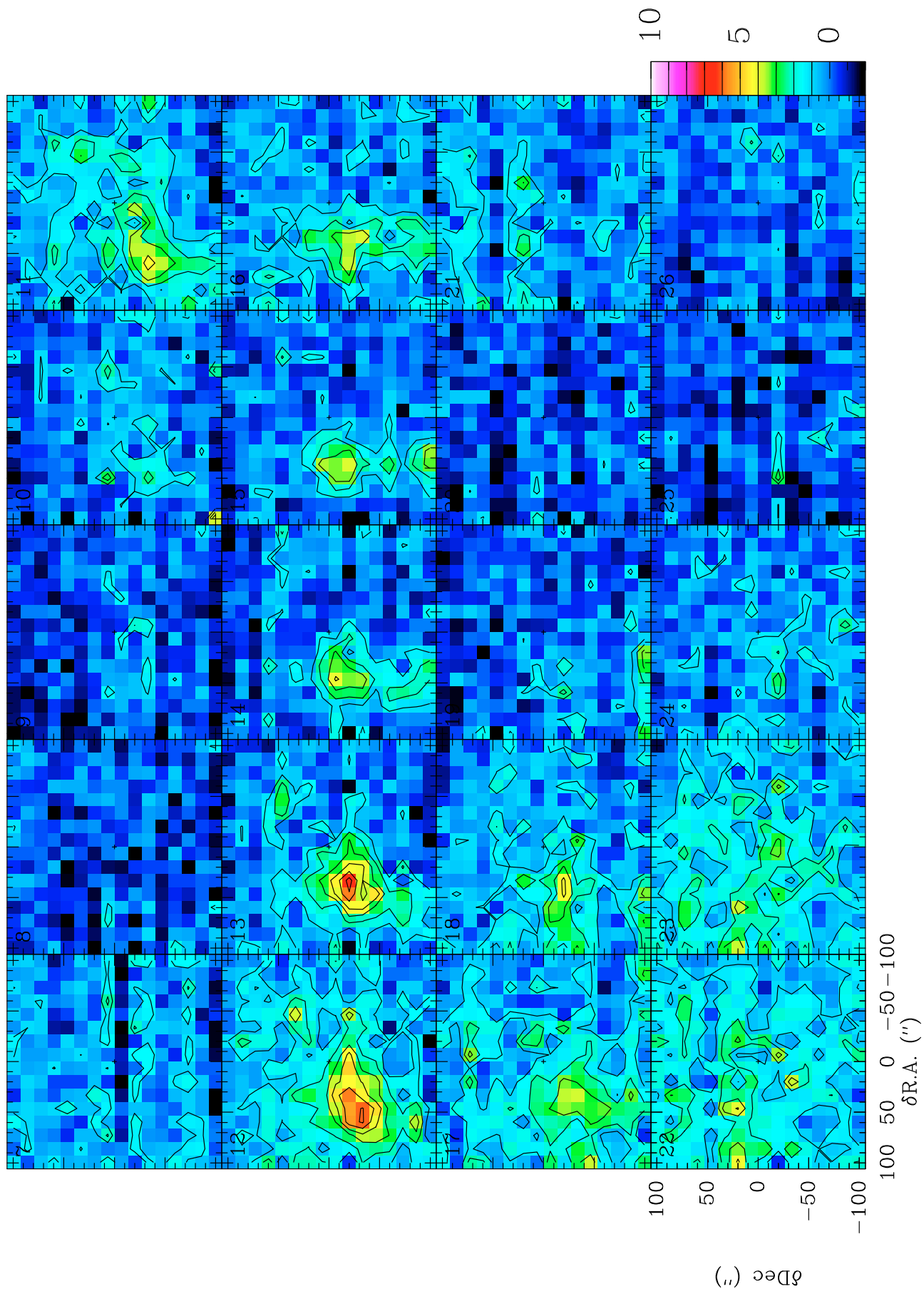
Fig. A.4. Velocity structure of the observed field: [CI] 2–1 intensity in velocity channels of 1 km s^{-1} width. Contours range between 1 and 10 K in steps of 1 K. The position $(0, 0)$ corresponds to RA(J2000.0) = 11$^{\rm h}$15$^{\rm m}$08$^{\rm s}$.85, Dec(J2000.0) = $-61°16'50''.0$.

References

Aumann, H., Fowler, J., & Melnyk, M. 1990, AJ, 99, 1674
Brandner, W., Grebel, E. K., Chu, Y.-H., et al. 2000, AJ, 119, 292
Crowther, P. A. 2007, ARA&A, 45, 177
Crowther, P. A., Schnurr, O., Hirschi, R., et al. 2010, MNRAS, 408, 731
Cubick, M., Stutzki, J., Ossenkopf, V., Kramer, C., & Röllig, M. 2008, A&A, 488, 623
Dale, J. E., Bonnell, I. A., Clarke, C. J., & Bate, M. 2005, MNRAS, 358, 291
Dedes, C., Röllig, M., Mookerjea, B., et al. 2010, A&A, 521, L24
Draine, B. T. 1978, ApJS, 36, 595
Frerking, M. A., Langer, W. D., & Wilson, R. W. 1982, ApJ, 262, 590
Frogel, J. A., Persson, S. E., & Aaronson, M. 1977, ApJ, 213, 723
Gorti, U., & Hollenbach, D. 2002, ApJ, 573, 215
Goss, W. M., & Radhakrishnan, V. 1969, Astrophys. Lett., 4, 199
Grabelsky, D. A., Cohen, R. S., Bronfman, L., & Thaddeus, P. 1988, ApJ, 331, 181
Harayama, Y., Eisenhauer, F., & Martins, F. 2008, ApJ, 675, 1319
Helou, G., Khan, I., Malek, L., & Boehmer, L. 1988, ApJ, 68, 151
Hollenbach, D. J., & Tielens, A. G. G. M. 1999, Rev. Mod. Phys., 71, 173
Ikeda, M., Oka, T., Tatematsu, K., Sekimoto, Y., & Yamamoto, S. 2002, ApJS, 139, 467
Kramer, C., Mookerjea, B., Bayet, E., et al. 2005, A&A, 441, 961
Kramer, C., Cubick, M., Röllig, M., et al. 2008, A&A, 477, 547
Lebouteiller, V., Brandl, B., Bernard-Salas, J., Devost, D., & Houck, J. R. 2007, ApJ, 665, 390
Lebouteiller, V., Bernard-Salas, J., Brandl, B., et al. 2008, ApJ, 680, 398
Martins, F., Schaerer, D., & Hillier, D. J. 2005, A&A, 436, 1049
Melena, N. W., Massey, P., Morrell, N. I., & Zangari, A. M. 2008, ApJ, 135, 878
Mookerjea, B., Kramer, C., Röllig, M., & Masur, M. 2006, A&A, 456, 235
Mücke, A., Koribalski, B. S., Moffat, A. F. J., Corcoran, M. F., & Stevens, I. R. 2002, ApJ, 571, 366
Müller, H. S. P., Thorwirth, S., Roth, D. A., & Winnewisser, G. 2001, A&A, 370, L49
Müller, H. S. P., Schlöder, F., Stutzki, J., & Winnewisser, G. 2005, J. Molec. Struct., 742, 215

Nakagawa, T., Yui, Y. Y., & Doi, Y., e. a. 1998, ApJS, 115, 259
Nürnberger, D. E. A. 2008, J. Phy. Conf. Ser., 131
Nürnberger, D. E. A., Bronfman, L., Yorke, H. W., & Zinnecker, H. 2002, A&A, 394, 253
Nürnberger, D. E. A., Vehoff, S., Hummel, C. A., & Duschl, W. J. 2010, Rev. Mex. Astron. Astrofis., 38, 71
Okada, Y., Kawada, M., Murakami, N., et al. 2010, A&A, 514, A13
Ossenkopf, V., Röllig, M., Simon, R., et al. 2010, 518, L79
Panagia, N. 1973, AJ, 78, 929
Pandey, A. K., Ogura, K., & Sekiguchi, K. 2000, PASJ, 52, 847
Pardo, J., Cernicharo, J., & Serabyn, E. 2001, IEEE Transactions on Antennas and Propagation, 49, 1683
Pauldrach, A. W. A., Lennon, M., Hoffmann, T. L., et al. 1998, in Properties of Hot Luminous Stars, ed. I. Howarth, ASP Conf. Ser., 131, 258
Rochau, B., Brandner, W., Stolte, A., et al. 2010, ApJ, 716, L90
Röllig, M., Ossenkopf, V., Jeyakumar, S., Stutzki, J., & Sternberg, A. 2006, A&A, 451, 917
Röllig, M., Abel, N. P., Bell, T., et al. 2007, A&A, 467, 187
Sakai, J. I., Nagasugi, Y., Saito, S., & Kaufmann, P. 2006, A&A, 457, 313
Shaver, P. A., & Goss, W. M. 1970, Austral. J. Phys. Astrophys. Suppl., 14, 133
Simon, R., Graf, U., Kramer, C., Stutzki, J., & Onishi, T. 2007, NANTEN technical report, 13.2.2007, 1, 1
Stacey, G. J., Geis, N., Genzel, R., et al. 1991, ApJ, 373, 423
Stolte, A., Brandner, W., Brandl, B., Zinnecker, H., & Grebel, E. K. 2004, AJ, 128, 765
Stolte, A., Brandner, W., Brandl, B., & Zinnecker, H. 2006, AJ, 132, 253
Störzer, H., Stutzki, J., & Sternberg, A. 1996, A&A, 310, 592
Stutzki, J., & Winnewisser, G. 1985, A&A, 144, 13
Sun, K., Ossenkopf, V., Kramer, C., et al. 2008, A&A, 489, 207
Sung, H., & Bessell, M. S. 2004, AJ, 127, 1014
Tatematsu, K., Jaffe, D. T., Plume, R., Evans, II, N. J., & Keene, J. 1999, ApJ, 526, 295
Wang, J., & Chen, Y. 2010, Sci. China G: Phys. Astron., 53, 271
Zinnecker, H., & Yorke, H. W. 2007, ARA&A, 45, 481